Peroxymonosulfate Activation by Co-Doped Magnetic Mn3O4 for Degradation of Oxytetracycline in Water

Liyan He
Lanzhou University
Hui Li
Wuhan Institute of Technology
Jianzhi Wang
Wuhan Institute of Technology
Qifei Gao
Lanzhou University
Xiaoli Li (lixiaoli@lzu.edu.cn)
Lanzhou University https://orcid.org/0000-0002-4797-8271

Research Article

Keywords: Fe3O4/Co-Mn3O4, OTC, Catalytic degradation, PPCPs, Wastewater treatment

Posted Date: October 29th, 2021

DOI: https://doi.org/10.21203/rs.3.rs-946361/v1

Version of Record: A version of this preprint was published at Environmental Science and Pollution Research on January 31st, 2022. See the published version at https://doi.org/10.1007/s11356-022-18929-1.

Peroxymonosulfate activation by Co-doped magnetic Mn_3O_4 for degradation of oxytetracycline in water

Liyan He[a], Hui Li[b], Jianzhi Wang[b], Qifei Gao[a], Xiaoli Li[a]*

[a]*Gansu Key Laboratory for Environmental Pollution Prediction and Control, College of Earth and Environmental Sciences, Lanzhou University, Lanzhou, 730000, China*

[b]*Key Laboratory for Green Chemical Process of Ministry of Education, School of Chemical Engineering and Pharmacy, Wuhan Institute of Technology, Wuhan,430205, China*

ABSTRACT

Co-doped magnetic Mn_3O_4 was synthesized by the solvothermal method and adopted as an effective catalyst for the degradation of oxytetracycline (OTC) in water. Synergistic interactions between Co-Mn_3O_4 and Fe_3O_4 not only resulted in the enhanced catalytic activity through the activation of peroxymonosulfate (PMS) to degrade OTC, but also made Fe_3O_4/Co-Mn_3O_4 easy to be separated and recovered from aqueous solution. 94.2% of OTC could be degraded within 60 min at an initial OTC concentration of 10 mg/L, catalyst dosage of 0.2 g/L and PMS concentration of 10 mM, the high efficiency of which was achieved in a wider pH range of 3.0-10.0. The free radical quenching experiments showed that $O_2^{\bullet-}$ radicals and $^1O_2$ played the main role in the degradation process. Co^{3+}, Co^{2+}, Fe^{2+}, Fe^{3+}, Mn^{4+}, Mn^{3+} and Mn^{2+} on Fe_3O_4/Co-Mn_3O_4 were identified as catalytic sites based on XPS analysis. Eventually, the intermediates of OTC degradation were examined and the possible decomposition pathways were proposed. The excellent catalytic performance of Fe_3O_4/Co-Mn_3O_4 not

*Corresponding author. Tel.: +86 931 8912404.
E-mail address: lixiaoli@lzu.edu.cn (X. Li).

only came from the fact that the large specific surface area could provide abundant active sites for the activation of PMS, but also the charged redistribution among atoms to accelerate the reduction of metal ions. The high degradation efficiency of OTC in actual water samples indicated that Fe_3O_4/Co-Mn_3O_4 had good potential for practical application.

Keywords: Fe_3O_4/Co-Mn_3O_4, OTC, Catalytic degradation, PPCPs, Wastewater treatment

1. Introduction

With people's increasing attention to environmental health, pharmaceutical and personal care products (PPCPs) are widely used in medicines to prevent and treat human and animal diseases and as personal care products in daily life [1, 2], resulting in the discharge of a large amount of wastewater containing PPCPs and their metabolites into the environment. PPCPs have been considered as one of the emerging pollutants and one of the biggest culprits affecting the water environment [3-5]. Therefore, there is increasing concern about the harmful impacts of PPCPs and their metabolites on microorganisms [6, 7], plants [8], animals [9] and human beings [10-12].

As a semisynthetic antibiotic, oxytetracycline (OTC) is widely used as an antimicrobial agent due to its good compatibility and low cost. However, OTC will eventually enter the natural water bodies in various ways because it is difficult to be absorbed by the digestive tract [13]. The OTC exposure to the water environment will have an impact on the flora, fauna and even the ecosystem. The long-term OTC exposure not only altered the intestinal microbiome of zebrafish but also altered thyroid hormone and serotonin homeostasis in zebrafish [14]. Moreover, OTC had photoinduced toxicity to *Daphnia magna* (Crustacea, Cladocera) and microalgae *Raphidocelis subcapitata* (Chlorophyceae) under ultraviolet or visible short-wave radiation [15]. Therefore, it is imperative to explore economical and efficient

technologies for the removal of OTC in water. At present, there have been many reports on the methods of removing OTC from water bodies. At present, the methods to remove oxytetracycline from water mainly include physical adsorption [16], Fenton - like oxidation [17], electrochemical catalytic oxidation [18], photocatalysis [19], etc.

Sulfate radical-based advanced oxidation processes (SR-AOPs) are widely used for oxidizing and degrading pollutants [20]. SR-AOPs can produce highly reactive species that react directly with pollutants to oxidize them into less toxic compounds even harmless small molecule compounds such as CO_2 and H_2O. The $SO_4^{\bullet-}$ and $^{\bullet}OH$ radicals produced by SR-AOPs exhibit excellent oxidation capacity in wastewater treatment owing to their higher oxidation potential (2.5-3.1 V and 1.8-2.7 V *vs*. NHE, respectively) [21, 22], high selectivity and wide pH response range. In general, $SO_4^{\bullet-}$ radical is produced via peroxymonosulfate (PMS) activation with various activation methods, such as heat [23], UV [24, 25], electro-activation [26], transition metal [27, 28] and ultrasound [29]. The transition metal activation is usually used because of its low equipment requirements, low cost and more flexibility.

Zero-valent transition metals and their ions (Co^{2+}, Cu^{2+}, Mn^{2+}, Ni^{2+}, Fe^{2+}, Fe^{3+}, etc.) are often used for the activation of PMS to oxidize pollutants. Among them, Mn_3O_4 is concerned because they contain multiple valence states [30]. The rapid redox transformation between Mn^{2+}, Mn^{3+} and Mn^{4+} plays a key role in the activation of the Mn_3O_4-PMS system [31, 32]. However, there are still limits on its aggressive catalytic capacity and application performances, which limit its further application to some extent. At present, the optimized methods include carbon-encapsulated [33], incorporating a metal-organic skeleton [34], doping more active metal ions, etc. [35]. Among them, doping metal ions such as Co, Ni, Zn, Cu, Fe, Cr, etc. are more feasible due to their high catalytic activity and wide availability. Co has been considered to be the most effective PMS activator where Co^{2+} is transformed to Co^{3+} and then to Co^{2+} regeneration [36, 37]. Ren et al. found that $CoFe_2O_4$ exhibited the highest catalytic capability to activate PMS for the degradation of DBP, which was higher than that of $CuFe_2O_4$, $MnFe_2O_4$ and $ZnFe_2O_4$ [38]. However, the separation and recovery of highly effective catalyst are very important. Although the carbon coating and

metal-organic framework used in the above literature promoted the catalytic efficiency of PMS, they did not solve the difficult problem of separation and recovery from aqueous solution. The best way to address this issue is to introduce magnetic particles to endow catalyst with magnetic response. Compared to other magnetic nanoparticles, nano-Fe_3O_4 with a larger specific surface area can provide more contact area and active sites for PMS activation, and make the removal of pollutants have a higher effect [39, 40]. More importantly, Fe_3O_4 can be prepared by rapid chemical precipitation and its synthesis is simple.

In this study, a Co-doped Mn_3O_4 magnetic nanocatalyst was synthesized by a solvothermal method. The addition of highly active metal Co could change the distribution of electric charge and the electron density, thus significantly improving the catalytic performance of the material. Meanwhile, magnetic Fe_3O_4 nanoparticles were loaded on the material to add the active sites and facilitate the rapid separation and recovery of the material from aqueous solution. Therefore, a new type of multifunctional Fe_3O_4/Co-Mn_3O_4 nanocatalyst was prepared. The synthesized catalyst would possess rapid magnetic separation and excellent performance in activating PMS. OTC, a common spectral antibiotic, was selected as the target pollutant, and the effects of the dosage of catalyst, solution pH, initial OTC concentration and salt concentration were studied. The free radical quenching experiments were carried out to identify the active species in the catalytic process. Then, to further analyze the degradation mechanisms, the OTC conversion products were analyzed by high-resolution mass spectrometry. Finally, the reusability and stability of Fe_3O_4/Co-Mn_3O_4 and its potential application in actual water samples were discussed.

2. Experimental section

2.1. Materials

Iron trichloride ($FeCl_3 \cdot 6H_2O$), ferrous chloride ($FeCl_2 \cdot 4H_2O$), cobalt chloride ($CoCl_2 \cdot 6H_2O$) and ethyl alcohol (C_2H_6O, ≥99%) were purchased from Damao

Chemical Reagent Factory (Tianjin, China). Manganese acetate (Mn $(CH_3COO)_2$, ≥98%) was supplied by Kaixin Chemical Industry Co. Ltd (Tianjin, China).

2.2. Synthesis of Fe_3O_4/Co-Mn_3O_4 nanocomposites

The traditional chemical precipitation process of Fe_3O_4 was as follows: First, 5.4059 g $FeCl_3 \cdot 6H_2O$ was dissolved in 25 mL of water and injected with nitrogen. After stirring for 30 min, 25 mL aqueous solution of $FeCl_2 \cdot 4H_2O$ (1.9881 g) was added to the above solution and stirred for another 30 min. Following, 25 mL of 10 M NaOH was dripped slowly and kept stirring for 1 h. Finally, the mixture was heated to 90℃ and lasted for 2 h. The product was separated using a magnet and washed with deionized water until the pH was neutral. The final precipitate was dried at 60℃.

The synthetic process of Fe_3O_4/Co-Mn_3O_4 was conducted according to the literature with some modification [41]: Firstly, 0.1401 g of Fe_3O_4 was added into 50 mL ethanol aqueous solution (the volume ratio of water: ethanol = 1:24) and stirred. Subsequently, 0.9804 g of Mn $(CH_3COO)_2$ and 0.0327 g of $CoCl_2 \cdot 6H_2O$ were added under continuous rapid stirring. Finally, 5 mL, 10 mM of potassium hydroxide solution was dropped into the solution and stirred vigorously for 10 min. The final mixed solution was transferred to a Teflon stainless steel autoclave and maintained at 175℃ for 60 min. The products cooled down to room temperature and washed with acetone for one time, a mixture of methanol and acetone (v: v=10:75) three times, and finally dried at 60℃. The synthesizing process of Fe_3O_4/Co-Mn_3O_4 was displayed in Scheme 1.

2.3. Characterization of catalysts

The morphology features of Fe_3O_4 and Fe_3O_4/Co-Mn_3O_4 were characterized by scanning electron microscope (SEM, JSM-5600LV) and their crystal structure and dimensions used transmission electron microscope (TEM, TECNAI G2 TF 20). A specific surface area and pore size distribution analyzer (Micromeritic Chemisorb 2750) was used to acquire the N_2 absorption-desorption curves. X-ray diffraction

(XRD) patterns and crystal structure changes before and after catalysis of the prepared materials were obtained via X-ray diffractometer (XRD, Rigaku D/MAX-2400 X-ray diffractometer). Fourier transform infrared spectroscopy (FTIR, Nicolet NEXUS 670) was applied to obtain the absorption spectra of Fe_3O_4 and Fe_3O_4/Co-Mn_3O_4 before and after catalysis of OTC under the range from 400 to 4000 cm^{-1}. The changes in the binding energy of the material before and after the catalysis of OTC were analyzed by X-ray photoelectron spectroscopy (XPS, PHI-5702). The magnetic properties of the Fe_3O_4 and Fe_3O_4/Co-Mn_3O_4 were calculated using a vibrating sample magnetometer (VSM, LAKESHORE-7304). The leaching rate of metal ions (Fe, Co, Mn) after the reaction was determined by inductively coupled plasma-optical emission spectroscopy (ICP-OES, Plasma Quant PQ9000).

2.4. Catalytic activity of Fe_3O_4/Co-Mn_3O_4

Batch experiments were conducted to study the activation of PMS by Fe_3O_4/Co-Mn_3O_4 where OTC was selected as the target organic pollutant. The catalytic activity was investigated by adding 0.02 g catalyst and 10 mM PMS into 10 mg/L OTC solution at its natural pH value and the reaction lasted for 60 min. All experiments were carried out in a thermostatic oscillator at 180 rpm and 20℃. To ensure the high-efficiency of the catalyst and the effective utilization of active sites, the dosage of the catalyst was adjusted from 0.01 to 0.03 g. The initial pH value of the OTC solutions was adjusted from 3.0 to 10.0 to explore the influence of pH on the catalytic activity. The initial pH values of the solutions were adjusted with 0.1 mol/L of NaOH or HCl solution. The influence of initial OTC concentrations ranging from 10 to 100 mg/L was investigated. The effect of salt was studied by adding 0.1 M NaCl, $NaHCO_3$, and $NaNO_3$ into the OTC solution. Moreover, the concentration of NaHA was 0.1 g/L.

To further investigate the active species in the degradation process of OTC, free radical quenching experiments were carried out. The hydroxyl radical ($^{\bullet}OH$) and sulfate radical ($SO_4^{\bullet-}$) were cleared with methyl alcohol (MeOH, 10 mM). The

hydroxyl radical ($^{\bullet}OH$), superoxide radical ($O_2^{\bullet-}$), and singlet oxygen ($^1O_2$) in the reaction system were eliminated by adding 10 mM of isopropanol (i-PrOH), 1, 4 -Benzoquinone (BQ) and furfuryl alcohol (FFA), respectively.

Using a UV-Vis spectrophotometer (CAM UV300) to determine the residual concentration of OTC at 350 nm. The removal efficiency (%) of OTC by Fe_3O_4/Co-Mn_3O_4 was measured based on the following equation:

$$RE(\%) = (C_0 - C_t) / C_0 \times 100\% \quad (1)$$

where C_0 (mg/L) and C_t (mg/L) are the concentrations of OTC at initial and t min in solution, respectively.

In this study, the pseudo-first-order model was used to describe the catalytic rate of OTC by Fe_3O_4/Co-Mn_3O_4. The kinetic equation was expressed as follows [42]:

$$\ln(C_t/C_0) = -k_{obs} \cdot t \quad (2)$$

where $\mathbf{k}_{obs}$ is the catalytic rate constant (min^{-1}).

The intermediate products of the OTC catalytic reaction were determined by mass spectrometry. The mineralization of OTC was obtained by measuring the removal rate of total organic carbon (TOC).

3. Results and discussion

3.1 Characterization of as-prepared samples

The microstructure characteristics of the as-prepared samples were well displayed by SEM (Fig. 1a-d) and TEM (Fig. 1e-h). The SEM results showed that the surface of Fe_3O_4 and Fe_3O_4/Co-Mn_3O_4 were rough, and Fe_3O_4 was closely attached to the surface of Co-Mn_3O_4. We could clearly conclude from Fig. 1c and d, pure Mn_3O_4 had both cubic and spherical structures, and the surface tended to be smooth after doping Co ions. As could be seen from the TEM pictures, the particle size of Fe_3O_4 was 5-20 nm and the particle size of Fe_3O_4/Co-Mn_3O_4 was 10-25 nm. In addition, the HRTEM lattice fringes 0.247 and 0.309 nm of Fig. 1g and h correspond to (211) and

(112) crystal planes in Mn_3O_4, respectively. The element distribution on the material surface was detected, and the results in Fig. 1i-l showed that Fe, Co, Mn, and O elements were evenly distributed on the Fe_3O_4/Co-Mn_3O_4 surface.

The N_2 adsorption and desorption curves were shown in Fig. 2a. It was obvious that the adsorption-desorption curves of Mn_3O_4, Co-Mn_3O_4, Fe_3O_4 and Fe_3O_4/Co-Mn_3O_4 presented hysteresis, and their hysteresis loop appeared to be a H4-type, which indicated that Mn_3O_4, Co-Mn_3O_4, Fe_3O_4 and Fe_3O_4/Co-Mn_3O_4 were mesoporous solid mediums. As shown in Table 1, the specific surface area, pore size and pore volume of pure Fe_3O_4 was 128.6 m^2/g, 11.10 nm and 0.36 cm^3/g, respectively, and these values further decreased to 93.49 m^2/g, 10.53 nm and 0.25 cm^3/g after the introduction of Co-Mn_3O_4, which might be due to that the Co-Mn_3O_4 occupied part of surfaces and channels of the material. These results suggested that the Fe_3O_4/Co-Mn_3O_4 possessed high specific surface area and interpenetrating channels, which would provide more active sites and facilitate the diffusion of the target molecules into the interior.

XRD was carried out to identify the phase information of Fe_3O_4 and Fe_3O_4/Co-Mn_3O_4. As shown in Fig. 2b, Fe_3O_4 at 30.0°, 35.6°, 43.2°, 57.2°, and 62.3° respectively denoted its (220), (311), (400), (511) and (440) crystal faces (based on PDF#19-0629) [43]. By comparing with PDF standard card, the XRD characteristic diffraction peaks of Mn_3O_4 were completely consistent with the PDF standard card of Mn_3O_4 (based on PDF#24-0734). Among them, the peaks at 18.0°, 28.9°, 31.0°, 32.3°, 36.1°, 37.9°, 44.4°, 50.7°, 58.5°, 59.8°and 64.7° represented the crystal faces of (101), (112), (200), (103), (211), (004), (220), (105), (321), (224) and (400), respectively, [41]. The illustration in Fig. 2b expressed a decrease in the intensity of the Mn peak where Co was introduced, and the XRD diffraction peaks of Mn_3O_4 had a shift of 0.1-0.2° after Co doping, which revealed that Co was doped into Mn_3O_4. Meanwhile, as could be seen from the XRD illustration, the diffraction peaks intensity of pure Mn_3O_4 and Mn_3O_4 doped with Co were very high. After loading magnetic Fe_3O_4, the diffraction peaks intensity decreased significantly, but the characteristic diffraction peaks were still obvious. This indicated that the material was successfully obtained.

The functional groups on Fe_3O_4 and Fe_3O_4/Co-Mn_3O_4 were authenticated with FTIR (Fig. 2c). There was broad absorption band from 3200 to 3600 cm^{-1} which represented the stretching vibration of free surface water. The characteristic peak at 1627 cm^{-1} could be assigned to the H-O-H stretching vibration of water absorption on Fe_3O_4. Fe_3O_4 sample exhibited a peak at around 580 cm^{-1} attributing to the stretching vibration of the Fe-O bond [44]. The peaks located at around 623.5 cm^{-1} and 435 cm^{-1} were the characteristic absorption peaks of Mn_3O_4, representing the stretching vibration of tetrahedral sites for Mn-O bonds and the Mn-O stretching vibration modes of Mn^{3+} in tetrahedral, respectively [45]. Besides, the band at 1435.2 cm^{-1} could be ascribed to the bending vibration of hydroxyl combined with Mn atoms [46].

The results of magnetometer analysis of Fe_3O_4 and Fe_3O_4/Co-Mn_3O_4 were displayed in Fig. 2d. The Fe_3O_4 and Fe_3O_4/Co-Mn_3O_4 exhibited obvious superparamagnetism and ferromagnetic properties. The magnetic saturation intensity of Fe_3O_4 and Fe_3O_4/Co-Mn_3O_4 were 45.5 and 40.5 emu/g, respectively. Although the magnetic saturation intensity of Fe_3O_4/Co-Mn_3O_4 slightly decreased, it did not affect the rapid separation characteristics of the material, which helped to greatly reduce operation cost and improve separation efficiency.

3.2 Catalytic studies

3.2.1 Catalytic performances of as-prepared samples

The removal efficiencies of OTC under different conditions (PMS alone, Fe_3O_4+PMS, Fe_3O_4/Mn_3O_4+PMS, Co-Mn_3O_4+PMS, Mn_3O_4+PMS, Fe_3O_4/Co-Mn_3O_4 alone and Fe_3O_4/Co-Mn_3O_4+PMS) were exhibited in Fig. 3a. It was demonstrated that the adsorption of OTC by individual Fe_3O_4/Co-Mn_3O_4 was sufficiently visible. But this part of the adsorption proved contaminant molecules to adhere to the surface of the material, thus facilitating the degradation process. PMS alone, Fe_3O_4+PMS, Mn_3O_4+PMS and Fe_3O_4/Mn_3O_4+PMS could degrade OTC, and the removal efficiency achieved 45.50%, 67.89%, 81.55% and 67.97%, respectively, after 60 min. Co-Mn_3O_4 exhibited the highest catalytic capability to activate PMS, resulted in 96% degradation

of OTC and 0.1609 min^{-1} of rate constant, respectively, which were slightly higher than those of Fe_3O_4/Co-Mn_3O_4 (94.2% and 0.1371 min^{-1}, respectively). As shown in Fig. 1, the TEM results showed that the addition of Fe_3O_4 would cause some Co-Mn_3O_4 sites to be masked, resulting in a slight decrease in catalytic performance. Moreover, after the addition of Fe_3O_4, Fe_3O_4/Co-Mn_3O_4 could provide different catalytic sites (Fe, Mn, Co) to activate PMS for OTC degradation. In addition, the greater advantage of Fe_3O_4/Co-Mn_3O_4 was that it could quickly separate and recover catalysts from aqueous solutions with the help of magnets.

The catalytic performances of Fe_3O_4/Co-Mn_3O_4 with different contents of Fe_3O_4 and Co were further compared and the results were presented in Fig. 3c, d and Fig. 4a, b. When the content of Fe_3O_4 increased from 20% to 60%, the degradation efficiency and rate constant of OTC first increased and then decreased. While the degradation efficiency of OTC was not affected significantly with increasing Co content within 15%-30%. Therefore, Fe_3O_4/Co-Mn_3O_4 with 30% of Fe_3O_4 content and 20% of Co content was eventually selected for subsequent experiments.

3.2.2 The dosage of Fe_3O_4/Co-Mn_3O_4

As displayed in Fig. 4c and d, when the dosage of Fe_3O_4/Co-Mn_3O_4 was increased from 0.01 to 0.02 g, the degradation efficiency and rate constant of OTC were significantly enhanced. The increase in catalyst dosage meant more active sites for the activation of PMS, which resulted in a higher removal efficiency. However, the dosage of catalyst higher than 0.02 g did not further increase the degradation efficiency and rate constant of OTC due to a fixed PMS concentration. In consideration of degradation efficiency and operation cost, 0.02 g was finally adopted as the best dosage and used in subsequent experiments.

3.2.3 The impact of pH

The catalytic degradation of OTC was performed at different pH values. As shown in Fig. 5a and b, the degradation efficiency of OTC was between 82.41% and

94.2% under the given pH range of 3.0-10.0. It was noted that the maximum OTC degradation took place at pH 7.0 with a rate constant of 0.2280 min^{-1} and the slow OTC degradation occurred at pH 8.0 with a rate constant of 0.1723 min^{-1}. In acidic/neutral conditions and alkaline conditions, PMS existed in the form of HSO_5^- and SO_5^{2-}, respectively, and HSO_5^- had stronger oxidation capacity [47], so the catalytic rate of OTC would decrease in alkaline conditions. Moreover, under high pH conditions precipitation of Co $(OH)_2$ should also occur, which might lead to further degradation of catalytic activity. But in general, these results suggested that Fe_3O_4/Co-Mn_3O_4 could effectively activate PMS to degrade OTC in a wider pH range from near-neutral to weakly acidic conditions.

3.2.4 The effect of initial pollutant concentration and salts

As shown in Fig. 5c and d, both the degradation efficiency and rate constant of OTC decreased with the increasing of initial pollutant concentration from 10 to 100 mg/L. Therefore, the combination of Fe_3O_4/Co-Mn_3O_4 and PMS was favorable for the catalytic degradation of OTC at low concentrations. Salts such as NaCl, $NaHCO_3$, $NaNO_3$ and NaHA were used to investigate the effect of electrolytes. We could conclude from Fig. 6a that all of them promoted the degradation of OTC except $NaNO_3$, and $NaNO_3$ significantly inhibited the degradation of OTC.

In the traditional AOPs radical reaction, Cl^- was identified as a scavenger for $SO_4^{\bullet-}$ /$^{\bullet}OH$ because Cl^- could react with $SO_4^{\bullet-}$ and $^{\bullet}OH$ ($k_{Cl^-+SO_4^{\bullet-}} = 3.1\times10^8\ M^{-1}\ s^{-1}$, $k_{Cl^-+{}^{\bullet}OH} = 4.3\times10^9\ M^{-1}s^{-1}$) to form lower oxidation potential chloride radicals ($Cl^{\bullet}$) (Eq. (3)-(6)) which inhibited the degradation of OTC [47-50]. However, the addition of sodium chloride did not inhibit but promote the degradation process, indicating that $SO_4^{\bullet-}$ and $^{\bullet}OH$ free radicals were not the main active species in this reaction. At the same time, a high concentration of Cl^- greatly promoted the degradation of OTC, which was suggested to be due to the formation of active chlorine substances with higher oxidation capacity for OTC. And the result was consistent with the previous research [48].

The HCO_3^- could react with $SO_4^{\bullet-}$ ($k_{\bullet SO4-/HCO3-}$ = 2.8×10^6 M^{-1} s^{-1}) or $^{\bullet}OH$ ($k_{\bullet HO/HCO3-}$ = 8.6×10^6 M^{-1} s^{-1}) to form less reactive $HCO_3^{\bullet-}$ radicals (Eq. (7)-(8)) [51]. Besides, HCO_3^- could increase the pH value of the reaction, thus increasing the degree of OTC dissociation. Then, the metal cation of Fe_3O_4/Co-Mn_3O_4 bonded to the OTC surface through electrostatic attraction, increasing the removal of OTC, which was consistent with the results of pH analysis above [52].

$$Cl^- + SO_4^{\bullet-} \rightarrow SO_4^{2-} + Cl^{\bullet} \quad (3)$$

$$Cl^- + HSO_5^- \leftrightarrow SO_4^{2-} + HOCl \quad \text{(slow)} \quad (4)$$

$$H^+ + Cl^- + HClO \leftrightarrow H_2O + Cl_2 \quad \text{(fast)} \quad (5)$$

$$Cl^{\bullet} + Cl^{\bullet} \rightarrow Cl_2^{\bullet} \quad (6)$$

$$HCO_3^- + SO_4^{\bullet-} \rightarrow HCO_3^{\bullet-} + SO_4^{2-} \quad (7)$$

$$HCO_3^- + {}^{\bullet}OH \rightarrow HCO_3^{\bullet-} + OH^- \quad (8)$$

The degradation degree of OTC was significantly inhibited when NO_3^- was present in the solution. NO_3^- could react with $SO_4^{\bullet-}$ and $^{\bullet}OH$ to remove some $^{\bullet}NO_2$ free radicals (Eq. (9)-(10)), resulting in a decrease of catalytic performance. This was consistent with the results of previous studies [53].

$$SO_4^{\bullet-} + NO_3^- \rightarrow SO_4^{2-} + {}^{\bullet}NO_2 \quad (9)$$

$${}^{\bullet}OH + NO_3^- \rightarrow OH^- + {}^{\bullet}NO_2 \quad (10)$$

The isoelectric point of the material was 3.1 (Fig. S1), while the potential of OTC aqueous solution after addition of 0.1 M $NaNO_3$, NaCl, $NaHCO_3$ and NaHA was calculated as 14.8, -7.6, -20.6 and -39.3 mV, respectively. The addition of $NaNO_3$ inhibited the degradation of OTC, which indicated that after the addition of $NaNO_3$, the combination of the material part and NO_3^- appeared charge reversal, thus affecting the potential [54].

3.2.5 UV-Vis spectroscopic analysis

Fig. 6b showed the UV-vis spectra of Fe_3O_4/Co-Mn_3O_4 for catalytic degradation

of OTC in the presence of PMS. It could be seen that the maximum absorption peak of OTC expressed a significant decrease in the first 10 min, indicating that the as-prepared catalyst had excellent catalytic activity. However, the absorption spectrum in UV-vis region did not completely disappear and the characteristic absorption peak of OTC was shifted by 48 units after the end of the reaction, which suggested that OTC molecules were not completely mineralized by Fe_3O_4/Co-Mn_3O_4. Thus, the catalytic reaction of OTC produced intermediate products, which needed to be detected and analyzed by mass spectrometry.

3.2.6 Identification of reactive species

To explore the reactive species of Fe_3O_4/Co-Mn_3O_4 in the activation of PMS, free radical scavenging experiments were carried out and the results were demonstrated in Fig. 6c and d. The MeOH was often used as a scavenger of $SO_4^{\bullet-}$ ($k_{SO4\bullet-}$=1.6-7.7×10^7 M^{-1} s^{-1}) and $^{\bullet}OH$ ($k_{\bullet OH}$ =1.2-2.8×10^9 M^{-1} s^{-1}) radicals because it contained α-H which could react with these two free radicals [55]. The i-PrOH was used to scavenge $^{\bullet}OH$ ($k_{\bullet OH}$ =1.9×10^9 M^{-1} s^{-1}) [56] and BQ was used to scavenge $O_2^{\bullet-}$ radicals [57]. The addition of MeOH and i-PrOH inhibited the catalytic reaction slightly, while the addition of BQ strongly inhibited the catalytic degradation. When MeOH and i-PrOH were added, the $\mathbf{k}_{obs}$ value of OTC was 0.1071 and 0.0993 min^{-1} respectively, which was 4-5 times that of BQ and FFA. This indicated that $SO_4^{\bullet-}$ and $^{\bullet}OH$ radicals were not the main active species in the degradation process, while $O_2^{\bullet-}$ radical was the main active substance. To further identify the $^1O_2$ reactive species in the process (Eq. (11)-(12)), FFA ($k_{FFA+1O2}$ = 1.2×10^8 M^{-1} s^{-1}) [52] was added into the Fe_3O_4/Co-Mn_3O_4/PMS system as a typical $^1O_2$ scavenger.

$$HSO_5^- + SO_5^{2-} \rightarrow SO_4^{2-} + HSO_4^- + {}^1O_2 \quad (11)$$

$$O_2^{\bullet-} + H_2O \rightarrow 2HO^- + H_2O_2 + {}^1O_2 \quad (12)$$

$$O_2^{\bullet-} / {}^{\bullet}OH / SO_4^{\bullet-} / {}^1O_2 + pollutants \rightarrow degradationproducts \quad (13)$$

The ultimate results revealed that the catalytic activity was significantly inhibited

after FFA was added, which indicated that $^1O_2$ was the main active substance. It was also demonstrated that non-free radicals were involved in the degradation process of OTC.

3.2.7 Analysis of degradation intermediates and possible mechanism

The intermediate products of OTC degradation were authenticated by high-resolution mass spectrometry. According to the mass spectrum of OTC degradation, there were four possible degradation pathways were deduced (Scheme 2). Round 1: The intermediate P1 (m/z 279.16) was derived from OTC degradation, resulting from the loss of carbonyl, hydroxyl, methyl, and amino groups [61]. Round 2: The intermediate P2 (m/z 399.35) was derived from the breaking of hydroxyl, carbonyl and amino bonds in OTC [62]. Then, P2 lost two more methyl groups, and oxidized-dehydrogenate to get P3 (m/z 388.72) [63]. P3 was further removed from the hydroxyl group, carbonyl group, double bond, and amino group, and the carbonyl group was hydrogenated to produce P1. Round 3: P4 (m/z 455.12) was produced by OTC through the loss of an OH group [64]. P4 lost part of its functional group, oxidizes and then hydrogenated to form P1. Round 4: OTC first oxidized and lost part of the functional group to form P5 (m/z 355.07). P5 then degraded to produce P1. In addition, we analyzed the predictive and mutagenic toxicity of OTC degradation intermediates (Fig. S2). In the predicted toxicity (Fig. S2a), although the transformation products were relatively toxic, the toxicity of all the products except P1 and P3 showed a decrease from the toxicity of mutagenesis (Fig. S2b). Therefore, the toxicity of products after degradation was decreased.

XPS was employed to give insights into the chemical states and changes of the binding energy of elements before and after catalysis of OTC by Fe_3O_4/Co-Mn_3O_4 (Fig. 7). The peaks at 638.1, 639.1, 640.2, and 641.8 eV corresponded to Mn^{2+}, Mn^{3+}, Mn^{4+} and satellite peaks, respectively (Fig. 7b) [31]. After the catalytic reaction, the content of Mn^{3+} decreased by 12.36%, while the content of Mn^{2+} and Mn^{4+} increased slightly. Besides, the change of binding energy of Mn^{2+} (+0.88 eV), Mn^{3+} (+0.58 eV),

Mn^{4+} (-0.42 eV) was observed, indicated that Mn as active sites was involved in catalytic reaction. The peaks of Co^{2+} appeared at 777.9 and 793.3 eV, while the peaks of Co^{3+} appeared at 783.1 and 770.3 eV (Fig. 7c) [58]. After catalytic reaction, the content of Co^{2+} decreased from 57.49% to 39.07%, while that of Co^{3+} increased from 42.51% to 60.93%. The decrease of Co^{2+} content fully indicated that part of Co^{2+} was converted into Co^{3+}, suggesting the occurrence of electron transfer within the metal. At the same time, the binding energy of both Co^{2+} (+1.32 eV) and Co^{3+} (+1.29-1.5 eV) increased after the reaction. As shown in Fig. 7d, the element Fe2p was divided into four peaks. Among them, the peaks of 707.4 and 721.0 eV were attributed to Fe^{2+}, while the peaks of 709.2 and 723.3 eV were attributed to Fe^{3+}. Besides, the peak at 716.1 and 730.5 eV corresponded to the satellite peak [34]. After catalytic degradation of OTC, the binding energy of Fe^{3+} increased by 0.35 eV and the content of Fe^{3+} decreased by 5.64%. These results indicated that there were redox reactions between metals with different valence states [58, 59]. The cyclic redox reactions in the metal proved that the materials were not simply superimposed, but a synergistic catalytic effect among the metals.

The removal efficiency and mineralization of OTC under different contact time were shown in Fig. 8a. Obviously, with the extension of reaction time, both removal rate and TOC of OTC increased. However, the removal rate of TOC was merely 62.73%, revealing that OTC was not completely degraded into CO_2 and H_2O but converted into other intermediate products. According to the free-radical quenching experiments, the OTC degradation process included free radical degradation and non-free radical degradation (Eq. (13)). Among them, free radical degradation was that OTC molecules were first adsorbed onto the surface of Fe_3O_4/Co-Mn_3O_4 and then degraded by $SO_4^{\bullet-}$ or $^{\bullet}OH$ free radicals. Through a non-radical pathway, PMS (as an electron acceptor) formed an active complex on the OTC surface (as an electron intermediate bridge) with the sp^2-metal ion network, Lewis basic group (C=O), and the binding site on the OTC. Subsequently, the OTC was degraded directly by the reactive complex through an abstract electron process [60]. The possible degradation process of OTC was displayed in Fig. 9.

3.2.8 Reusability and stability of Fe_3O_4/Co-Mn_3O_4

The Fe_3O_4/Co-Mn_3O_4s could be quickly recovered from aqueous solution by permanent magnets before each recycling. The reusability of Fe_3O_4/Co-Mn_3O_4 was studied as shown in Fig. 8b. It could be seen that the fresh Fe_3O_4/Co-Mn_3O_4 achieved 94.2% OTC removal within 60 min, while in the first run, 78.05% removal was achieved in 90 min. However, in the second, third and fourth run, the removal efficiencies were 73.84%, 75.44% and 72.69% when the reaction time was extended to 120 min, respectively. Meanwhile, the value of $\mathbf{k}_{obs}$ dropped from 0.1371 to 0.0317 min^{-1} as the number of cycles increased. This might be attributed to the accumulation of intermediates on the catalyst surface, the loss of catalyst, or the loss of metal active sites during the degradation, washing and drying of catalyst. Therefore, the catalytic performance of Fe_3O_4/Co-Mn_3O_4 would decrease with the cycle increased. However, the XRD pattern after the reaction was not significantly affected, indicating that the structure of the catalyst was relatively stable.

3.2.9 Practical application of Fe_3O_4/Co-Mn_3O_4

To further explore the potential of Fe_3O_4/Co-Mn_3O_4 in practical application, we sampled water bodies for the OTC degradation experiments. China's Yellow River located at the Zhongshan Bridge in Gansu Province was collected as actual water samples. It was observed from Fig. 8c, the characteristic peak of OTC in actual water samples dropped rapidly in the initial 1 min and shifted by 42 units after the reaction. The catalytic performances of Fe_3O_4/Co-Mn_3O_4 in actual water samples were also conducted at different catalyst dosage and initial OTC concentration. Compared with OTC removal in deionized water, high catalytic efficiency (about 98.8%) and rate constant of OTC in actual water samples could be achieved at low catalyst dosage of 15 mg (Fig. 8d). At the same time, the removal efficiency was reached up to 76.12% even at the OTC concentration of 50 mg/L (Fig. 8e). This fully proved that Fe_3O_4/Co-Mn_3O_4 still exhibited excellent catalytic ability to activate PMS for the degradation of OTC in actual water samples and had a great potential in practical

application.

4. Conclusion

Co-doped magnetic Mn_3O_4 (Fe_3O_4/Co-Mn_3O_4) was successfully prepared, characterized and applied to activate PMS for the degradation of OTC in aqueous solution. Fe_3O_4/Co-Mn_3O_4 expressed excellent catalytic ability and removed OTC in a wider pH range of 3.0-10.0, and the removal rate of OTC was as high as 94.2% under studied conditions. Moreover, the addition of NaCl, $NaHCO_3$ and NaHA effectively promoted the degradation of OTC. The degradation process was analyzed based on environmental condition control, rate constant calculation, free radical identification and product detection. The free radical quenching experiments showed that $O_2^{\bullet-}$ and $^1O_2$ played the main role in the degradation process of OTC, while $SO_4^{\bullet-}$ and $^{\bullet}OH$ played the minor role, which revealed that the degradation of OTC included free radical and non-free radical mechanisms. In the catalytic process, Co^{2+}, Co^{3+}, Fe^{2+}, Fe^{3+}, Mn^{2+}, Mn^{3+} and Mn^{4+} synergistically activated PMS to generate different kinds of free radicals, thus triggering the degradation of OTC. Besides, there was also a redox reaction between metals, and this internal metal cycle was conducive to the regeneration of active metal ions, which promoted the catalytic effect. The intermediate products were deduced by high-resolution mass spectrometry and the possible degradation mechanisms were proposed. Fe_3O_4/Co-Mn_3O_4 had good stability and reusability. Finally, highly efficient degradation of OTC in actual water samples suggested that Fe_3O_4/Co-Mn_3O_4 had a good potential in further application of wastewater treatment.

Funding

The authors gratefully acknowledge the financial supports from the Open Project of Key Laboratory of Green Chemical Engineering Process of Ministry of Education

(No. GCP20200207) and the Natural Science Foundation of Gansu Province (No. 20JR10RA631).

Availability of data and materials

Extra data are available from the authors (lixiaoli@lzu.edu.cn) upon reasonable request.

Authors' contributions

Xiaoli Li proposed the project and provided the funds. Liyan He designed the experiments and synthesized the materials. Liyan He did the series of experiments and prepared the first draft of this manuscript. Hui Li, Jianzhi Wang and Qifei Gao revised the manuscript. All co-authors contributed to this work.

Ethics statement

No animal studies are presented in this manuscript. No human studies are presented in this manuscript. No potentially identifiable human images or data are presented in this study.

Consent for participation

Not applicable.

Consent for publication

Not applicable.

Declaration of Interest Statement

The authors declare that they have no known competing financial interests or personal relationships that could have appeared to influence the work reported in this paper.

References

[1] Q.Q. Zhang, G.G. Ying, C.G. Pan, Y.S. Liu, J.L. Zhao, Comprehensive evaluation of antibiotics emission and fate in the river basins of China: Source analysis, multimedia modeling, and linkage to bacterial resistance, Environ. Sci. Technol. 49 (2015) 6772–6782. https://doi.org/10.1021/acs.est.5b00729.

[2] M. Hutchings, A. Truman, B. Wilkinson, Antibiotics: past, present and future, Curr. Opin. Microbiol. 51 (2019) 72–80. https://doi.org/10.1016/j.mib.2019.10.008.

[3] S. Shao, Y. Hu, J. Cheng, Y. Chen, Research progress on distribution, migration, transformation of antibiotics and antibiotic resistance genes (ARGs) in aquatic environment, Crit. Rev. Biotechnol. 38 (2018) 1195–1208. https://doi.org/10.1080/07388551.2018.1471038.

[4] Z. Xie, G. Lu, J. Liu, Z. Yan, B. Ma, Z. Zhang, W. Chen, Occurrence, bioaccumulation, and trophic magnification of pharmaceutically active compounds in Taihu Lake, China, Chemosphere. 138 (2015) 140–147. https://doi.org/10.1016/j.chemosphere.2015.05.086.

[5] G. Wang, S. Zhou, X. Han, L. Zhang, S. Ding, Y. Li, D. Zhang, K. Zarin, Occurrence, distribution, and source track of antibiotics and antibiotic resistance genes in the main rivers of Chongqing city, southwest China, J. Hazard. Mater. 389 (2020) 122110. https://doi.org/10.1016/j.jhazmat.2020.122110.

[6] B. Ferrari, R. Mons, B. Vollat, B. Fraysse, N. Paxéus, R. Lo Giudice, A. Pollio, J. Garric, Environmental risk assessment of six human pharmaceuticals: Are the current environmental risk assessment procedures sufficient for the protection of the aquatic environment?, Environ. Toxicol. Chem. 23 (2004) 1344–1354. https://doi.org/10.1897/03-246.

[7] C.H. Hagedorn, D.H. Alpers, Biodegradability of some antibiotics, elimination

of the genotoxicity and affection of wastewater bacteria in a simple test, Gastroenterology. 73 (1977) 1019–1022. https://doi.org/10.1016/s0016-5085(19)31851-7.

[8] N. Martins, R. Pereira, N. Abrantes, J. Pereira, F. Gonçalves, C.R. Marques, Ecotoxicological effects of ciprofloxacin on freshwater species: Data integration and derivation of toxicity thresholds for risk assessment, Ecotoxicology. 21 (2012) 1167–1176. https://doi.org/10.1007/s10646-012-0871-x.

[9] M. Isidori, M. Lavorgna, A. Nardelli, L. Pascarella, A. Parrella, Toxic and genotoxic evaluation of six antibiotics on non-target organisms, Sci. Total Environ. 346 (2005) 87–98. https://doi.org/10.1016/j.scitotenv.2004.11.017.

[10] R.R. Persaud, M.B. Azad, R.S. Chari, M.R. Sears, A.B. Becker, A.L. Kozyrskyj, Perinatal antibiotic exposure of neonates in Canada and associated risk factors: A population-based study, J. Matern. Neonatal Med. 28 (2015) 1190–1195. https://doi.org/10.3109/14767058.2014.947578.

[11] P. Zimmermann, N. Curtis, Effect of intrapartum antibiotics on the intestinal microbiota of infants: A systematic review, Arch. Dis. Child. Fetal Neonatal Ed. (2019) 1–8. https://doi.org/10.1136/archdischild-2018-316659.

[12] H. Chen, S. Liu, X.R. Xu, Z.H. Diao, K.F. Sun, Q.W. Hao, S.S. Liu, G.G. Ying, Tissue distribution, bioaccumulation characteristics and health risk of antibiotics in cultured fish from a typical aquaculture area, J. Hazard. Mater. 343 (2018) 140–148. https://doi.org/10.1016/j.jhazmat.2017.09.017.

[13] H. Hu, X. Li, S. Wu, W. Lou, C. Yang, Effects of long-term exposure to oxytetracycline on phytoremediation of swine wastewater via duckweed systems, J. Hazard. Mater. 414 (2021) 125508. https://doi.org/10.1016/j.jhazmat.2021.125508.

[14] J. Li, T. Dong, T.P. Keerthisinghe, H. Chen, M. Li, W. Chu, J. Yang, Z. Hu, S.A. Snyder, W. Dong, M. Fang, Long-term oxytetracycline exposure potentially alters brain thyroid hormone and serotonin homeostasis in zebrafish, J. Hazard. Mater. 399 (2020) 123061.

https://doi.org/10.1016/j.jhazmat.2020.123061.

[15] L. Peroti, P. Huovinen, S. Orellana, M. Muñoz, R. Fuentes, I. Gómez, Uptake of microalgae as sublethal biomarker reveals phototoxicity of oxytetracycline to the crustacean Daphnia magna, Water Res. 188 (2021) 116556. https://doi.org/10.1016/j.watres.2020.116556.

[16] Y. Li, M. Deng, X. Wang, Y. Wang, J. Li, S. Xia, J. Zhao, In-situ remediation of oxytetracycline and Cr(VI) co-contaminated soil and groundwater by using blast furnace slag-supported nanosized Fe^0/FeS_x, Chem. Eng. J. 412 (2021) 128706. https://doi.org/10.1016/j.cej.2021.128706.

[17] L. Li, S. Liu, M. Cheng, C. Lai, G. Zeng, L. Qin, X. Liu, B. Li, W. Zhang, Y. Yi, M. Zhang, Y. Fu, M. Li, M. Long, Improving the Fenton-like catalytic performance of MnO_x-Fe_3O_4/biochar using reducing agents: A comparative study, J. Hazard. Mater. 406 (2021) 124333. https://doi.org/10.1016/j.jhazmat.2020.124333.

[18] W. Ma, B. Yao, W. Zhang, Y. He, Y. Yu, J. Niu, Fabrication of PVDF-based piezocatalytic active membrane with enhanced oxytetracycline degradation efficiency through embedding few-layer E-MoS_2 nanosheets, Chem. Eng. J. 415 (2021) 129000. https://doi.org/10.1016/j.cej.2021.129000.

[19] W. Wang, Q. Niu, G. Zeng, C. Zhang, D. Huang, B. Shao, C. Zhou, Y. Yang, Y. Liu, H. Guo, W. Xiong, L. Lei, S. Liu, H. Yi, S. Chen, X. Tang, 1D porous tubular g-C_3N_4 capture black phosphorus quantum dots as 1D/0D metal-free photocatalysts for oxytetracycline hydrochloride degradation and hexavalent chromium reduction, Appl. Catal. B Environ. 273 (2020) 119051. https://doi.org/10.1016/j.apcatb.2020.119051.

[20] X. Lai, X. an Ning, J. Chen, Y. Li, Y. Zhang, Y. Yuan, Comparison of the Fe^{2+}/H_2O_2 and Fe^{2+}/PMS systems in simulated sludge: Removal of PAHs, migration of elements and formation of chlorination by-products, J. Hazard. Mater. 398 (2020) 122826. https://doi.org/10.1016/j.jhazmat.2020.122826.

[21] W. Da Oh, Z. Dong, T.T. Lim, Generation of sulfate radical through heterogeneous catalysis for organic contaminants removal: Current

development, challenges and prospects, Appl. Catal. B Environ. 194 (2016) 169–201. https://doi.org/10.1016/j.apcatb.2016.04.003.

[22] M. Kohantorabi, G. Moussavi, S. Giannakis, A review of the innovations in metal- and carbon-based catalysts explored for heterogeneous peroxymonosulfate (PMS) activation, with focus on radical vs. non-radical degradation pathways of organic contaminants, Chem. Eng. J. 411 (2020) 127957. https://doi.org/10.1016/j.cej.2020.127957.

[23] M. Nie, Y. Yang, Z. Zhang, C. Yan, X. Wang, H. Li, W. Dong, Degradation of chloramphenicol by thermally activated persulfate in aqueous solution, Chem. Eng. J. 246 (2014) 373–382. https://doi.org/10.1016/j.cej.2014.02.047.

[24] S. Karimian, G. Moussavi, F. Fanaei, S. Mohammadi, S. Shekoohiyan, S. Giannakis, Shedding light on the catalytic synergies between Fe(II) and PMS in vacuum UV (VUV/Fe/PMS) photoreactors for accelerated elimination of pharmaceuticals: The case of metformin, Chem. Eng. J. 400 (2020) 125896. https://doi.org/10.1016/j.cej.2020.125896.

[25] P. Chen, Y. Gou, J. Ni, Y. Liang, B. Yang, F. Jia, S. Song, Efficient Ofloxacin degradation with Co(II)-doped MoS_2 nano-flowers as PMS activator under visible-light irradiation, Chem. Eng. J. 401 (2020) 125978. https://doi.org/10.1016/j.cej.2020.125978.

[26] H. Lin, J. Wu, H. Zhang, Degradation of clofibric acid in aqueous solution by an EC/Fe^{3+}/PMS process, Chem. Eng. J. 244 (2014) 514–521. https://doi.org/10.1016/j.cej.2014.01.099.

[27] J. Zhao, F. Li, H. Wei, H. Ai, L. Gu, J. Chen, L. Zhang, M. Chi, J. Zhai, Superior performance of $ZnCoO_x$/peroxymonosulfate system for organic pollutants removal by enhancing singlet oxygen generation: The effect of oxygen vacancies, Chem. Eng. J. 409 (2021). https://doi.org/10.1016/j.cej.2020.128150.

[28] N. Jaafarzadeh, F. Ghanbari, M. Ahmadi, Efficient degradation of 2,4-dichlorophenoxyacetic acid by peroxymonosulfate/magnetic copper ferrite nanoparticles/ozone: A novel combination of advanced oxidation processes,

Chem. Eng. J. 320 (2017) 436–447. https://doi.org/10.1016/j.cej.2017.03.036.

[29] C. Cai, H. Zhang, X. Zhong, L. Hou, Ultrasound enhanced heterogeneous activation of peroxymonosulfate by a bimetallic Fe-Co/SBA-15 catalyst for the degradation of Orange II in water, J. Hazard. Mater. 283 (2015) 70–79. https://doi.org/10.1016/j.jhazmat.2014.08.053.

[30] E. Saputra, S. Muhammad, H. Sun, H.M. Ang, M.O. Tadé, S. Wang, Manganese oxides at different oxidation states for heterogeneous activation of peroxymonosulfate for phenol degradation in aqueous solutions, Appl. Catal. B Environ. 142–143 (2013) 729–735. https://doi.org/10.1016/j.apcatb.2013.06.004.

[31] F. Wang, M. Xiao, X. Ma, S. Wu, M. Ge, X. Yu, Insights into the transformations of Mn species for peroxymonosulfate activation by tuning the Mn_3O_4 shapes, Chem. Eng. J. 404 (2021) 127097. https://doi.org/10.1016/j.cej.2020.127097.

[32] R. Shokoohi, M. Salari, A. Shabanloo, N. Shabanloo, S. Marofi, H. Faraji, M. Vanaei Tabar, M. Moradnia, Catalytic activation of persulphate with Mn_3O_4 nanoparticles for degradation of acid blue 113: process optimisation and degradation pathway, Int. J. Environ. Anal. Chem. 00 (2020) 1–20. https://doi.org/10.1080/03067319.2020.1773810.

[33] Y. Liu, J. Luo, L. Tang, C. Feng, J. Wang, Y. Deng, H. Liu, J. Yu, H. Feng, J. Wang, Origin of the enhanced reusability and electron transfer of the carbon-coated Mn_3O_4 nanocube for persulfate activation, ACS Catal. 10 (2020) 14857–14870. https://doi.org/10.1021/acscatal.0c04049.

[34] J. Li, C., Wu, J., Peng, W., Fang, Z., & Liu, Peroxymonosulfate activation for efficient sulfamethoxazole degradation by Fe_3O_4/β-FeOOH nanocomposites: Coexistence of radical and non-radical reactions, Chem. Eng. J. 356 (2019) 904–914. https://doi.org/10.1016/j.cej.2018.09.064.

[35] Z.Y. Guo, C.X. Li, M. Gao, X. Han, Y.J. Zhang, W.J. Zhang, W.W. Li, Mn−O Covalency Governs the Intrinsic Activity of Co-Mn Spinel Oxides for Boosted Peroxymonosulfate Activation, Angew. Chemie - Int. Ed. 60 (2021) 274–280.

https://doi.org/10.1002/anie.202010828.

[36] X. Chen, J. Chen, X. Qiao, D. Wang, X. Cai, Performance of nano-Co_3O_4/peroxymonosulfate system: Kinetics and mechanism study using Acid Orange 7 as a model compound, Appl. Catal. B Environ. 80 (2008) 116–121. https://doi.org/10.1016/j.apcatb.2007.11.009.

[37] P. Hu, M. Long, Cobalt-catalyzed sulfate radical-based advanced oxidation: A review on heterogeneous catalysts and applications, Appl. Catal. B Environ. 181 (2016) 103–117. https://doi.org/10.1016/j.apcatb.2015.07.024.

[38] Y. Ren, L. Lin, J. Ma, J. Yang, J. Feng, Z. Fan, Sulfate radicals induced from peroxymonosulfate by magnetic ferrospinel MFe_2O_4 (M=Co, Cu, Mn, and Zn) as heterogeneous catalysts in the water, Appl. Catal. B Environ. 165 (2015) 572–578. https://doi.org/10.1016/j.apcatb.2014.10.051.

[39] Y. Zhang, B.T. Zhang, Y. Teng, J. Zhao, X. Sun, Heterogeneous activation of persulfate by carbon nanofiber supported Fe_3O_4@carbon composites for efficient ibuprofen degradation, J. Hazard. Mater. 401 (2021) 123428. https://doi.org/10.1016/j.jhazmat.2020.123428.

[40] H. Li, J. Wan, Y. Ma, Y. Wang, Synthesis of novel core–shell Fe^0@Fe_3O_4 as heterogeneous activator of persulfate for oxidation of dibutyl phthalate under neutral conditions, Chem. Eng. J. 301 (2016) 315–324. https://doi.org/10.1016/j.cej.2016.04.147.

[41] J.S. Hong, H. Seo, Y.H. Lee, K.H. Cho, C. Ko, S. Park, K.T. Nam, Nickel-Doping Effect on Mn_3O_4 Nanoparticles for Electrochemical Water Oxidation under Neutral Condition, Small Methods. 4 (2020) 1–7. https://doi.org/10.1002/smtd.201900733.

[42] C. Chen, M. Xie, L. Kong, W. Lu, Z. Feng, J. Zhan, Mn_3O_4 nanodots loaded g-C_3N_4 nanosheets for catalytic membrane degradation of organic contaminants, J. Hazard. Mater. 390 (2020) 122146. https://doi.org/10.1016/j.jhazmat.2020.122146.

[43] W. He, Z. Li, S. Lv, M. Niu, W. Zhou, J. Li, R. Lu, H. Gao, C. Pan, S. Zhang, Facile synthesis of Fe_3O_4@MIL-100(Fe) towards enhancing photo-Fenton like

degradation of levofloxacin via a synergistic effect between Fe_3O_4 and MIL-100(Fe), Chem. Eng. J. 409 (2021) 128274. https://doi.org/10.1016/j.cej.2020.128274.

[44] B. Peng, T. Song, T. Wang, L. Chai, W. Yang, X. Li, C. Li, H. Wang, Facile synthesis of Fe_3O_4@$Cu(OH)_2$ composites and their arsenic adsorption application, Chem. Eng. J. 299 (2016) 15–22. https://doi.org/10.1016/j.cej.2016.03.135.

[45] N. Li, Y. Tian, J. Zhao, J. Zhang, J. Zhang, W. Zuo, Y. Ding, Efficient removal of chromium from water by Mn_3O_4@ZnO/Mn_3O_4 composite under simulated sunlight irradiation: Synergy of photocatalytic reduction and adsorption, Appl. Catal. B Environ. 214 (2017) 126–136. https://doi.org/10.1016/j.apcatb.2017.05.041.

[46] J. Zhao, J. Nan, Z. Zhao, N. Li, J. Liu, F. Cui, Energy-efficient fabrication of a novel multivalence Mn_3O_4-MnO_2 heterojunction for dye degradation under visible light irradiation, Appl. Catal. B Environ. 202 (2017) 509–517. https://doi.org/10.1016/j.apcatb.2016.09.065.

[47] J. Luo, S. Bo, Y. Qin, Q. An, Z. Xiao, S. Zhai, Transforming goat manure into surface-loaded cobalt/biochar as PMS activator for highly efficient ciprofloxacin degradation, Chem. Eng. J. 395 (2020) 125063. https://doi.org/10.1016/j.cej.2020.125063.

[48] Z. Zeng, A. Khan, Z. Wang, M. Zhao, W. Mo, Z. Chen, Elimination of atrazine through radical/non-radical combined processes by manganese nano-catalysts/PMS and implications to the structure-performance relationship, Chem. Eng. J. 397 (2020) 125425. https://doi.org/10.1016/j.cej.2020.125425.

[49] Y. Yang, G. Banerjee, G.W. Brudvig, J.H. Kim, J.J. Pignatello, Oxidation of Organic Compounds in Water by Unactivated Peroxymonosulfate, Environ. Sci. Technol. 52 (2018) 5911–5919. https://doi.org/10.1021/acs.est.8b00735.

[50] Z.Y. Li, L. Wang, Y.L. Liu, P.N. He, X. Zhang, J. Chen, H.T. Gu, H.C. Zhang, J. Ma, Overlooked enhancement of chloride ion on the transformation of reactive species in peroxymonosulfate/Fe(II)/NH_2OH system, Water Res. 195

(2021) 116973. https://doi.org/10.1016/j.watres.2021.116973.

[51] J. Ali, A. Shahzad, J. Wang, J. Ifthikar, W. Lei, G.G. Aregay, Z. Chen, Z. Chen, Modulating the redox cycles of homogenous Fe(III)/PMS system through constructing electron rich thiomolybdate centres in confined layered double hydroxides, Chem. Eng. J. 408 (2021) 127242. https://doi.org/10.1016/j.cej.2020.127242.

[52] X. He, K.E. O'Shea, Selective oxidation of H1-antihistamines by unactivated peroxymonosulfate (PMS): Influence of inorganic anions and organic compounds, Water Res. 186 (2020) 116401. https://doi.org/10.1016/j.watres.2020.116401.

[53] Q.T. Sun, B. De Xu, J. Yang, T.T. Qian, H. Jiang, Layered oxides supported Co-Fe bimetal catalyst for carbamazepine degradation via the catalytic activation of peroxymonosulfate, Chem. Eng. J. 400 (2020). https://doi.org/10.1016/j.cej.2020.125899.

[54] Y. Wang, W. Zhang, J. Zhang, W. Sun, R. Zhang, H. Gu, Fabrication of a novel polymer-free nanostructured drug-eluting coating for cardiovascular stents, ACS Appl. Mater. Interfaces. 5 (2013) 10337–10345. https://doi.org/10.1021/am403365j.

[55] S. Liu, Z. Zhang, F. Huang, Y. Liu, L. Feng, J. Jiang, L. Zhang, F. Qi, C. Liu, Carbonized polyaniline activated peroxymonosulfate (PMS) for phenol degradation: Role of PMS adsorption and singlet oxygen generation, Appl. Catal. B Environ. 286 (2021) 119921. https://doi.org/10.1016/j.apcatb.2021.119921.

[56] Y. Liu, X. He, Y. Fu, D.D. Dionysiou, Degradation kinetics and mechanism of oxytetracycline by hydroxyl radical-based advanced oxidation processes, Chem. Eng. J. 284 (2016) 1317–1327. https://doi.org/10.1016/j.cej.2015.09.034.

[57] X. He, K.E. O'Shea, Rapid transformation of H1-antihistamines cetirizine (CET) and diphenhydramine (DPH) by direct peroxymonosulfate (PMS) oxidation, J. Hazard. Mater. 398 (2020) 123219. https://doi.org/10.1016/j.jhazmat.2020.123219.

[58] J. Jiang, X. Wang, C. Zhang, T. Li, Y. Lin, T. Xie, S. Dong, Porous 0D/3D $NiCo_2O_4$/g-C_3N_4 accelerate emerging pollutant degradation in PMS/vis system: Degradation mechanism, pathway and toxicity assessment, Chem. Eng. J. 397 (2020) 125356. https://doi.org/10.1016/j.cej.2020.125356.

[59] N. Liu, N. Lu, H.T. Yu, S. Chen, X. Quan, Degradation of aqueous bisphenol A in the CoCN/Vis/PMS system: Catalyst design, reaction kinetic and mechanism analysis, Chem. Eng. J. 407 (2021). https://doi.org/10.1016/j.cej.2020.127228.

[60] V.L. Pham, D.G. Kim, S.O. Ko, Advanced oxidative degradation of acetaminophen by carbon catalysts: Radical vs non-radical pathways, Environ. Res. 188 (2020) 109767. https://doi.org/10.1016/j.envres.2020.109767.

[61] Y. Yang, G. Zeng, D. Huang, C. Zhang, D. He, C. Zhou, W. Wang, W. Xiong, X. Li, B. Li, W. Dong, Y. Zhou, Molecular engineering of polymeric carbon nitride for highly efficient photocatalytic oxytetracycline degradation and H_2O_2 production, Appl. Catal. B Environ. 272 (2020) 118970. https://doi.org/10.1016/j.apcatb.2020.118970.

[62] C. Zhang, D. He, S. Fu, G. Zeng, Q. Liang, Silver iodide decorated ZnSn $(OH)_6$ hollow cube : Room-temperature preparation and application for highly efficient photocatalytic oxytetracycline degradation, Chem. Eng. J. 421 (2021) 129810. https://doi.org/10.1016/j.cej.2021.129810.

[63] X. Hu, C. Li, J. Song, S. Zheng, Z. Sun, Multidimensional assembly of oxygen vacancy-rich amorphous TiO_2-BiOBr-sepiolite composite for rapid elimination of formaldehyde and oxytetracycline under visible light, J. Colloid Interface Sci. 574 (2020) 61–73. https://doi.org/10.1016/j.jcis.2020.04.035.

[64] C.H. Han, H.D. Park, S.B. Kim, V. Yargeau, J.W. Choi, S.H. Lee, J.A. Park, Oxidation of tetracycline and oxytetracycline for the photo-Fenton process: Their transformation products and toxicity assessment, Water Res. 172 (2020) 115514. https://doi.org/10.1016/j.watres.2020.115514.

Figures

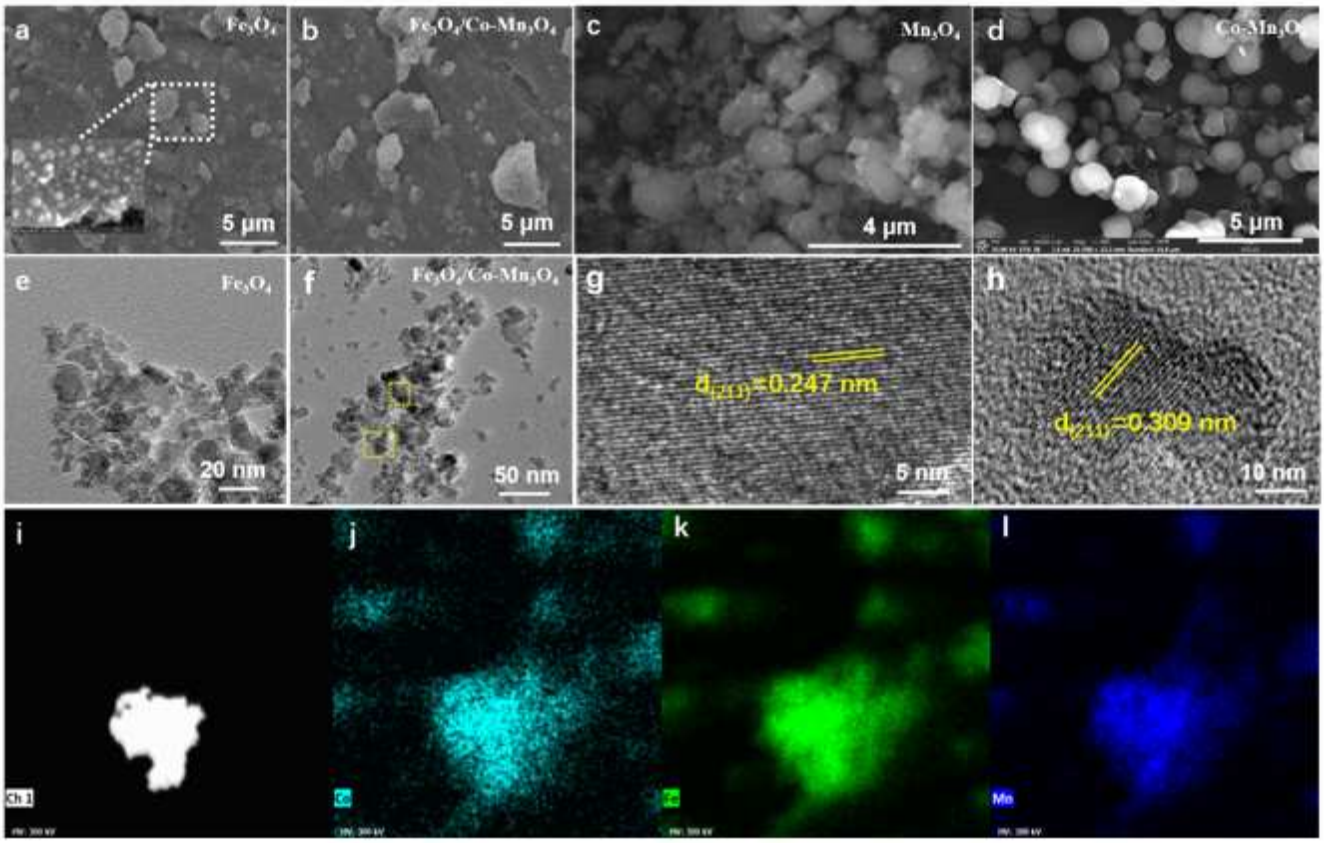

Fig. 1.

Figure 1

The SEM images of Fe3O4 (a) and Fe3O4/Co-Mn3O4 (b); TEM images of Fe3O4 (c)and Fe3O4/Co-Mn3O4 (d); SEM images of Mn3O4 (e) and Co-Mn3O4 (f); and the elemental mapping (Fe, Co and Mn elements) of Fe3O4/Co-Mn3O4 (g-j).

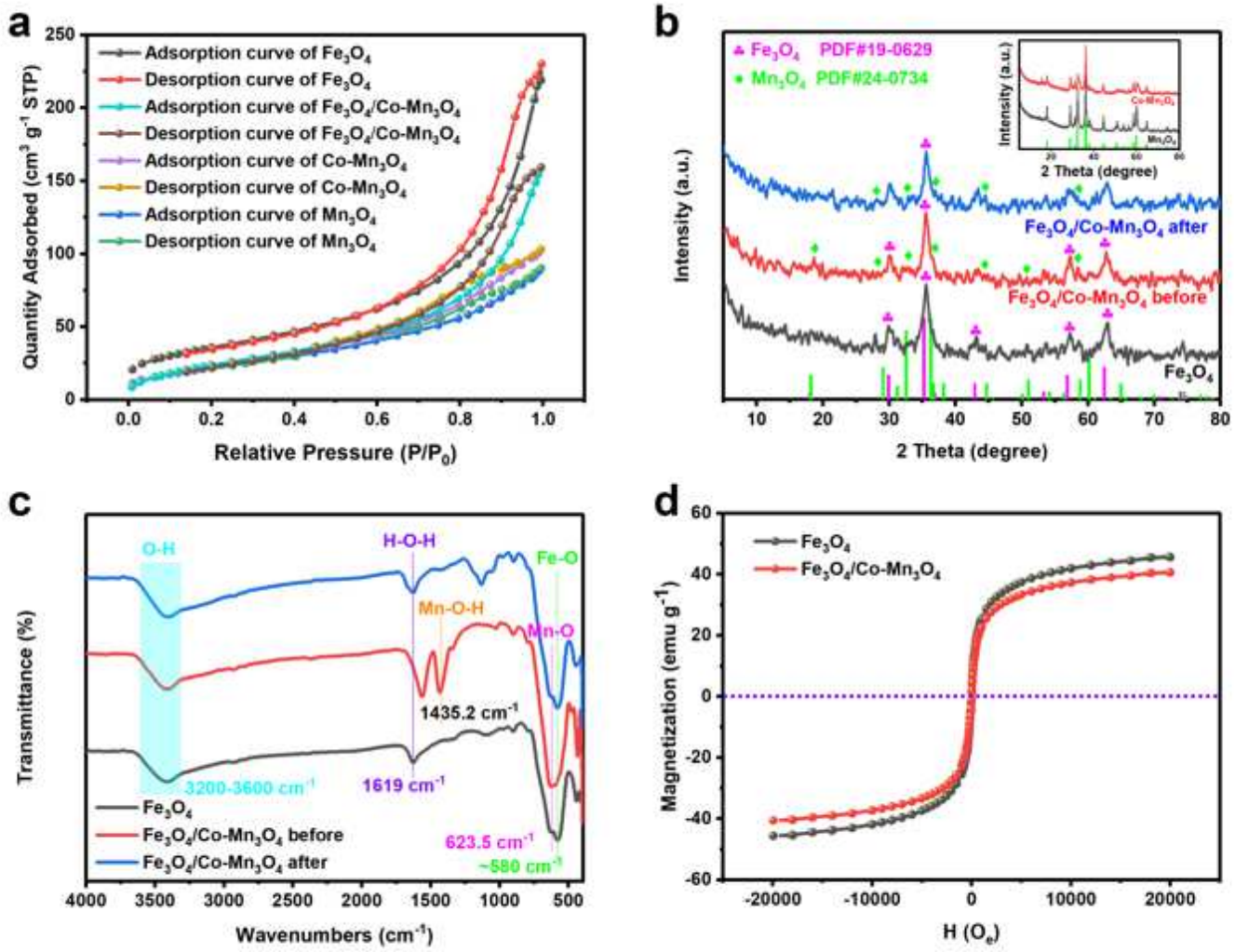

Fig. 2.

Figure 2

The N2 adsorption-desorption isotherms of Fe3O4, Mn3O4, Co-Mn3O4 and Fe3O4/Co-Mn3O4 (a); XRD patterns of Fe3O4, Fe3O4/Co-Mn3O4 (b) and the illustration were XRD patterns of Mn3O4 and Co-Mn3O4; FTIR spectra of Fe3O4 and Fe3O4/Co-Mn3O4 before OTC degradation and the FTIR spectra of Fe3O4/Co-Mn3O4 after OTC degradation (c); Magnetization curves of Fe3O4 and Fe3O4/Co-Mn3O4 (d).

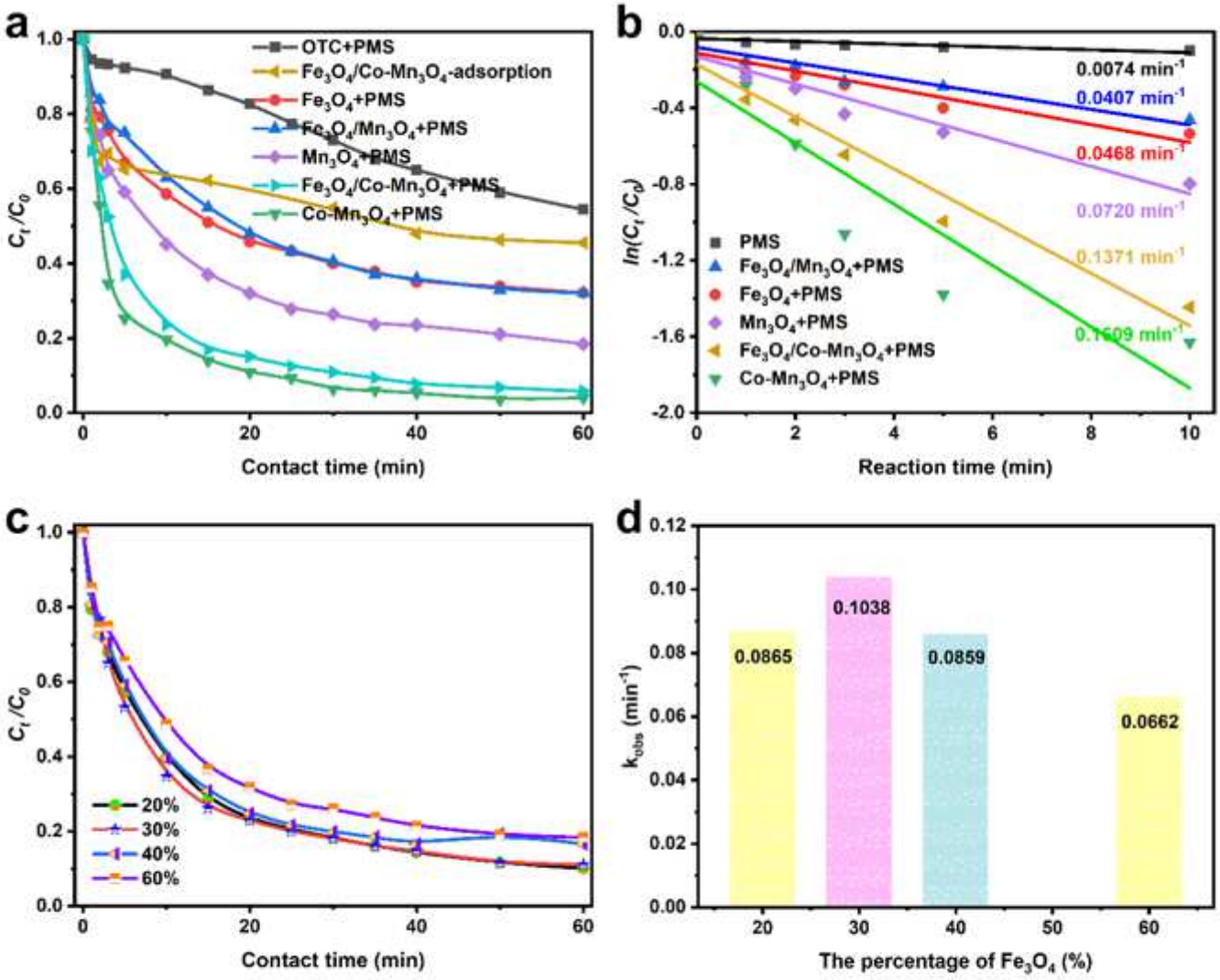

Fig. 3.

Figure 3

The comparison diagram of different components (a) and its kinetic fitting curve (b); the optimization of different Fe3O4 contents (c) and their rate constant kobs (d).

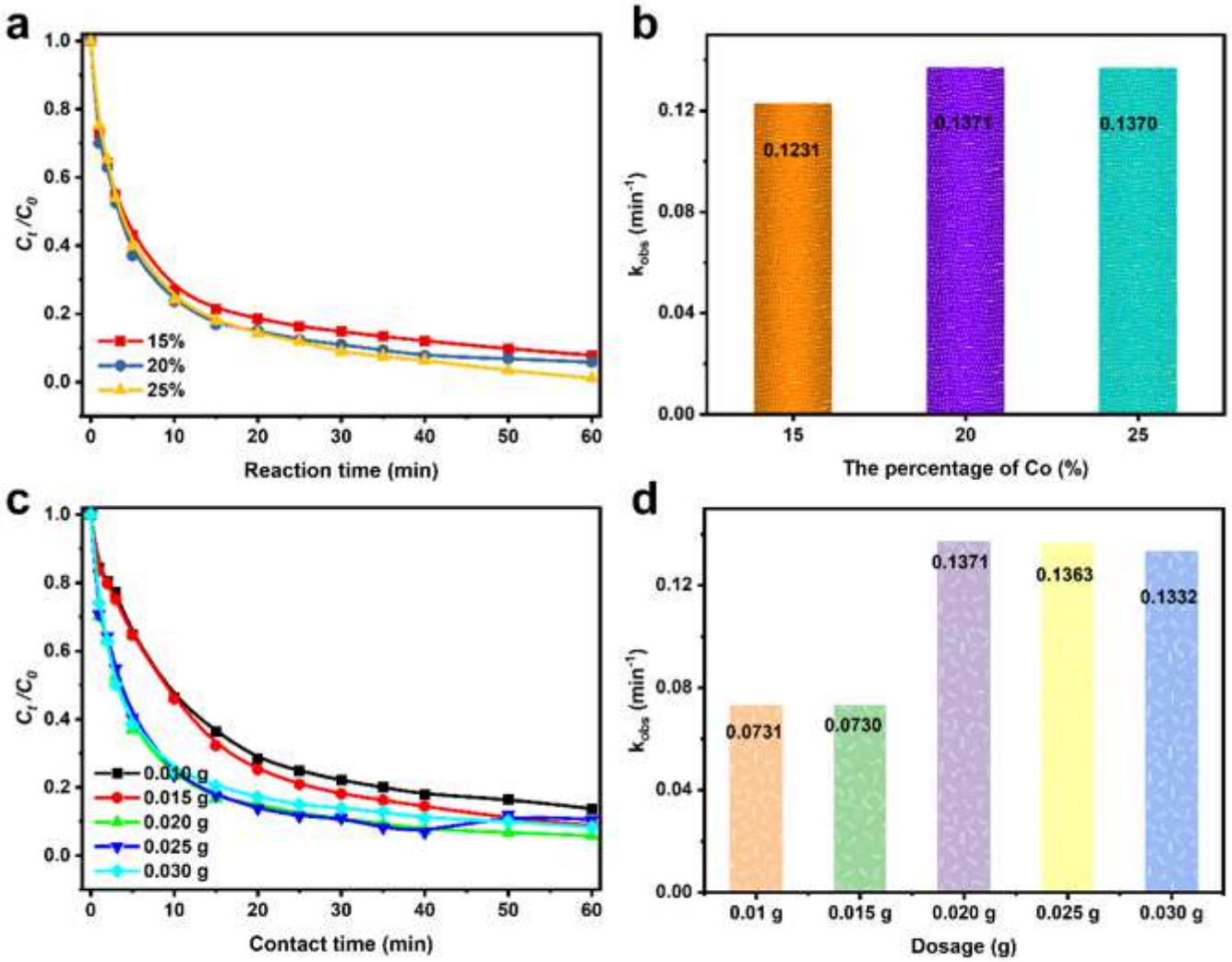

Fig. 4.

Figure 4

The optimization of different Co contents (a) and their rate constant kobs (b); the (Ct/C0) -t curves of different dosing amounts (c) and their rate constant kobs (d).

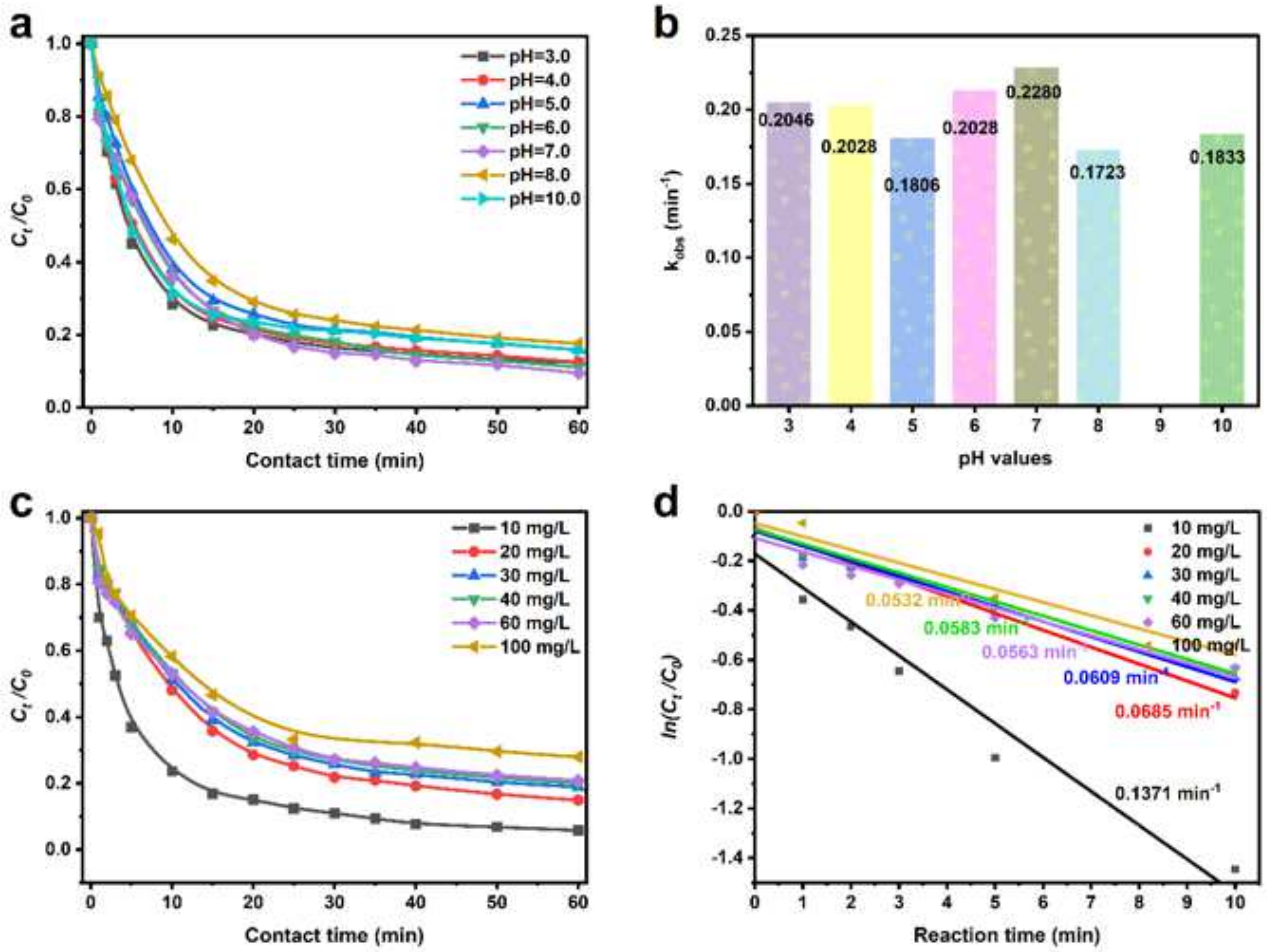

Fig. 5.

Figure 5

The (Ct/C0) -t curves of different pH values (a) and their rate constant kobs (b); the (Ct/C0) -t curves of different pH values (c), their kinetic fitting (d).

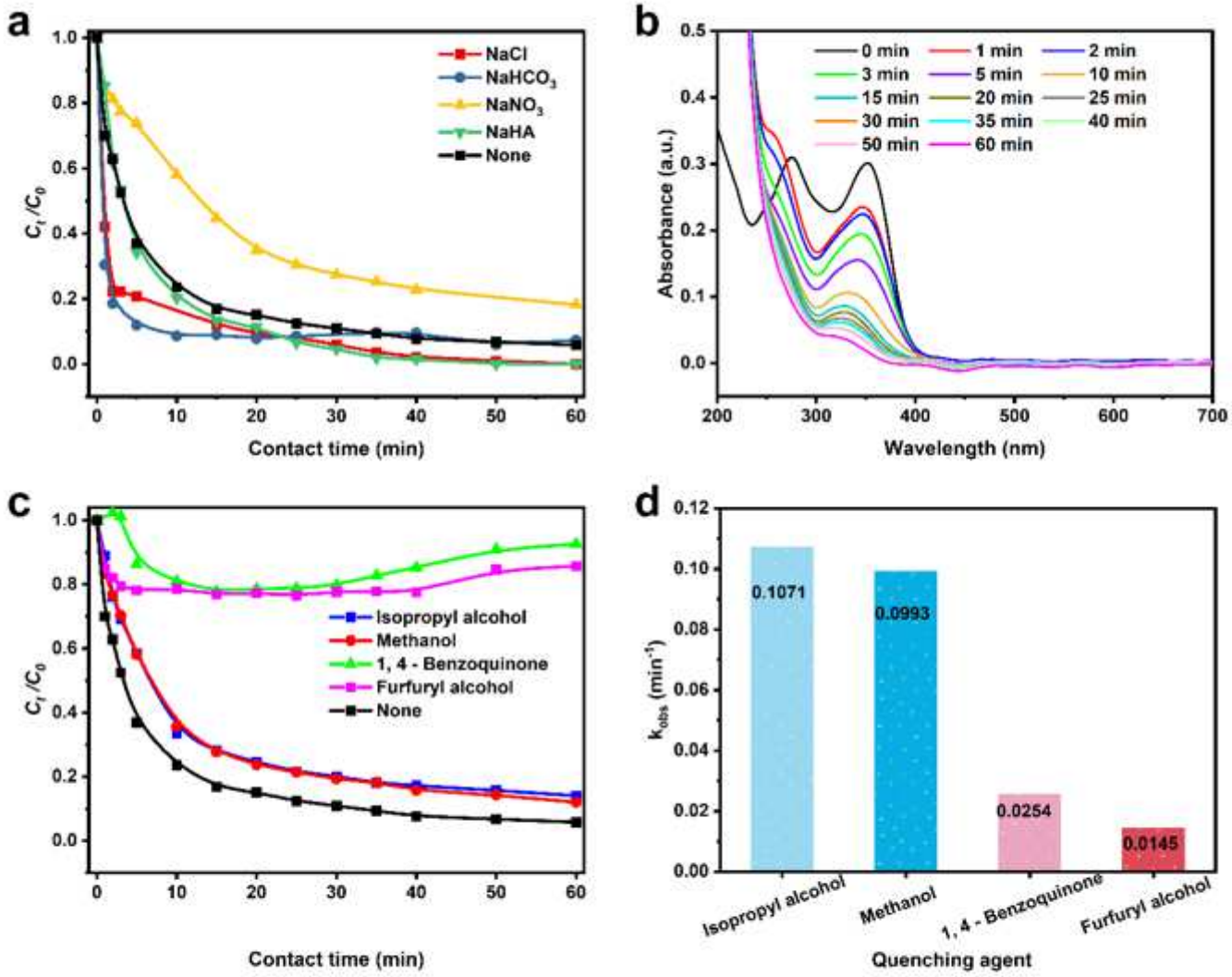

Fig. 6.

Figure 6

and effects of water background compounds (a); the UV-vis absorption spectra of OTC at 350 nm (b); the free radical quenching experiment (c) and their rate constant kobs (d).

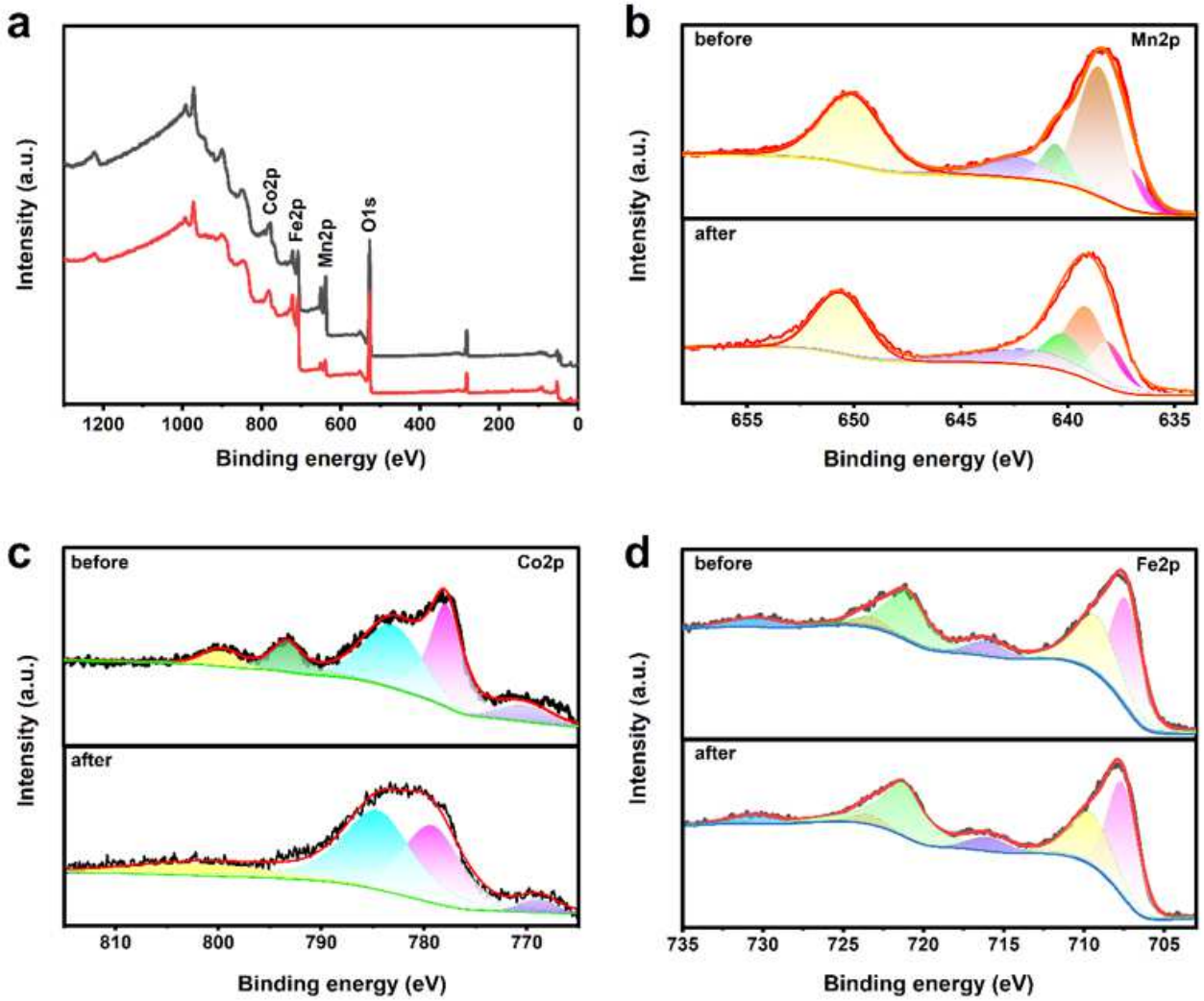

Fig. 7.

Figure 7

XPS total absorption peak spectra before and after catalysis (a), and XPS absorption peak spectra of Mn (b), Co (c) and Fe (d) element before and after catalysis.

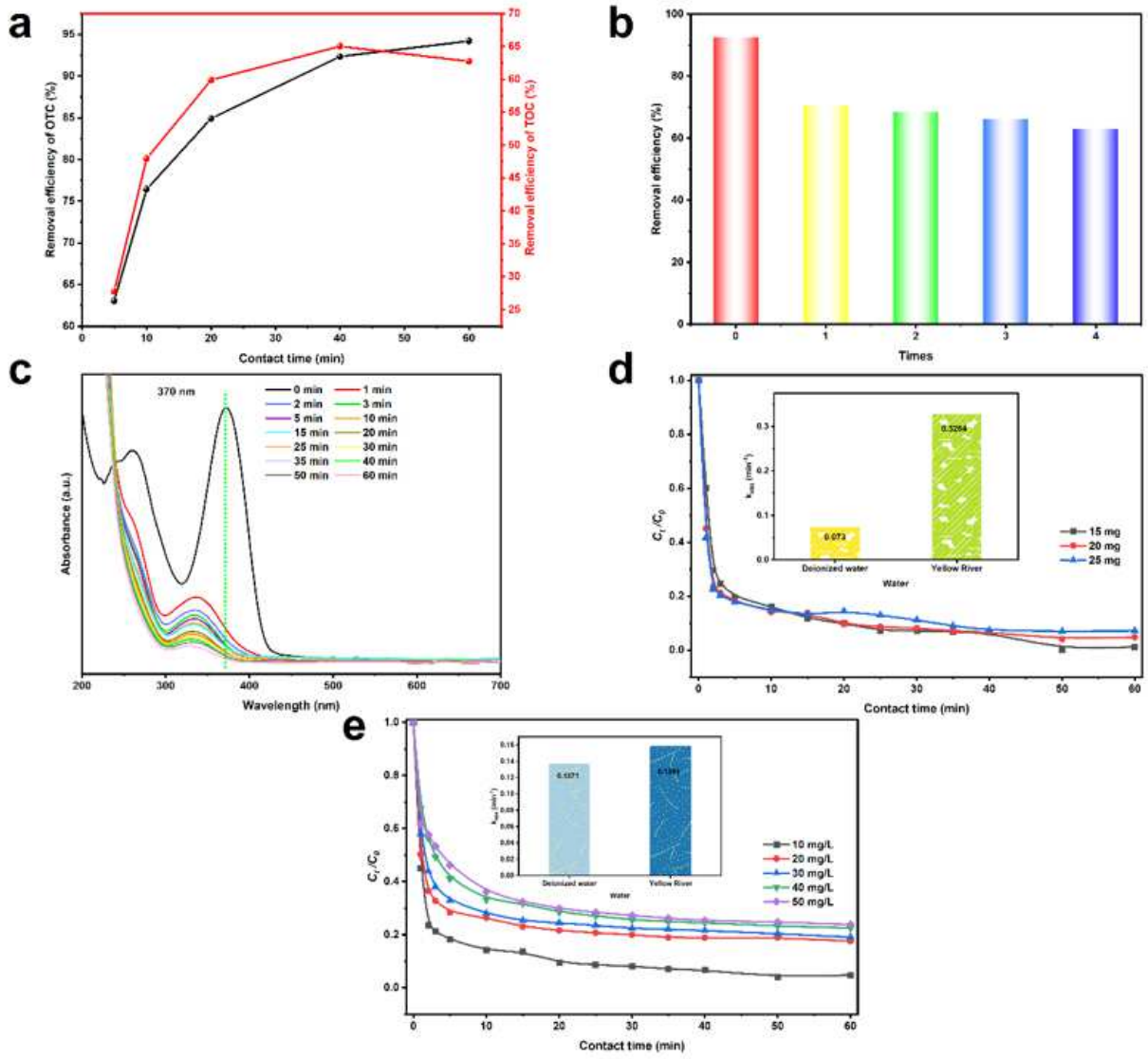

Fig. 8.

Figure 8

The removal efficiency of OTC and TOC (a); the reuse experiment (b); catalysis spectra (c) of Yellow River water, the changes of dosage (d) (the illustration showed the rate constant of Yellow River and deionized water at 15 mg), and concentration (e) (the illustration showed the rate constant of Yellow River and deionized water at 20 mg and 10 mg/L).

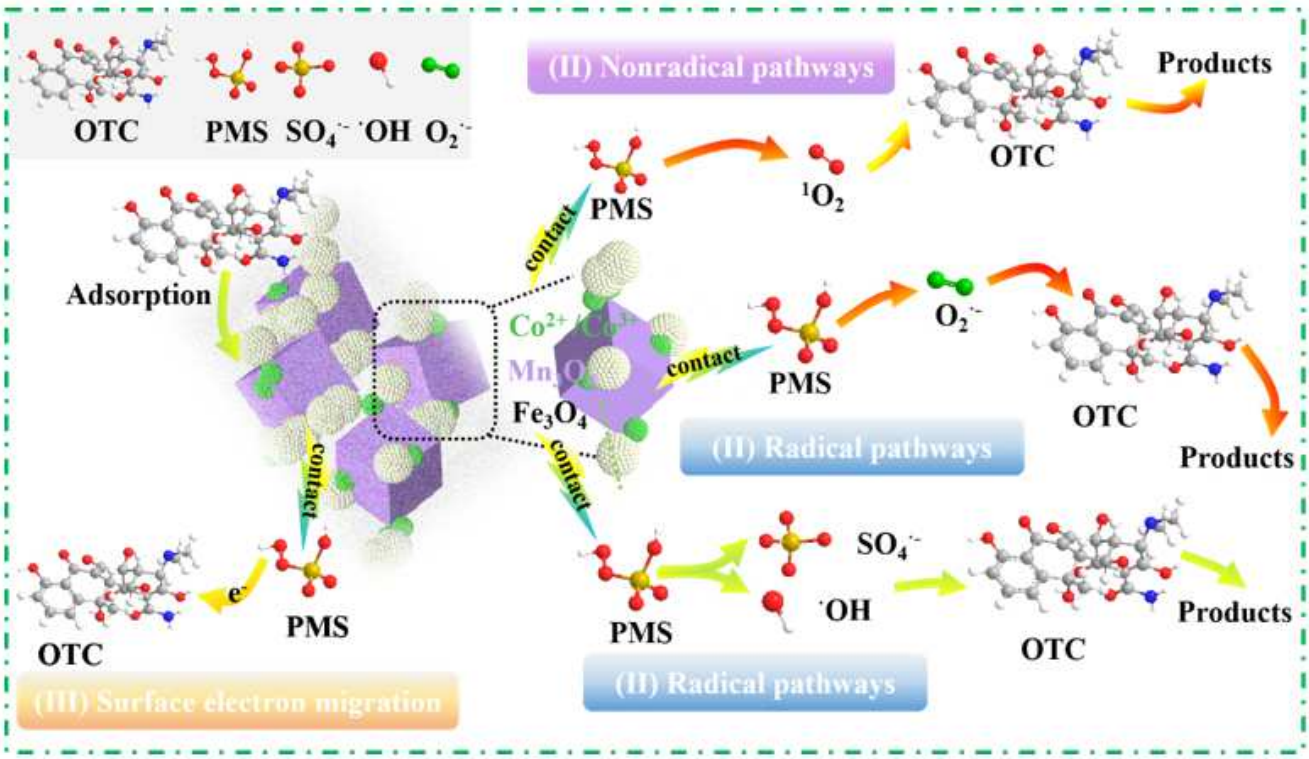

Fig. 9.

Figure 9

The possible degradation process of OTC.

Supplementary Files

This is a list of supplementary files associated with this preprint. Click to download.

- Scheme1.png
- Scheme2.png
- supplementarymaterial.docx